Inkjet Printing of Cobalt Ferrite for Hard Ferromagnetic Thick Films Manufacturing

Marco Mariani,* Francesco Cervellera, Emanuele Migliori, Federico Maspero, Roberto Bernasconi, Carmen Galassi, Luca Magagnin, and Nora Lecis

Inkjet printing is a versatile and cheap technique for the fabrication of films, offering unique advantages in terms of scalability, precision, and customization. In recent years, there has been a growing interest in utilizing inkjet printing technology for the deposition of magnetic films with tailored properties. Cobalt ferrite ($CoFe_2O_4$) stands out due to its exceptional magnetic properties, including high coercivity, saturation magnetization, and excellent chemical stability. This paper presents a comprehensive study on the inkjet printing of cobalt ferrite magnetic films, focusing on the manufacturing process, especially on the different factors that could lead to stable multilayer depositions to achieve high thicknesses: ink solid loading, drop spacing, substrate temperature, and interlayers drying. Finally, the microstructure of the samples is investigated to identify the occurring defects after sintering between 800 and 1000 °C. The magnetic properties of the films are determined, revealing a maximum coercivity of 1.98 kOe and a magnetic saturation of 78.25 emu cm^{-3}.

1. Introduction

Cobalt ferrite has gathered considerable attention as a promising material for magnetic film applications. It is a spinel ferrite possessing a unique combination of high magnetization, chemical stability, and magnetostriction properties.[1–3] These features

M. Mariani, F. Cervellera, E. Migliori, C. Galassi, N. Lecis
Department of Mechanical Engineering
Politecnico di Milano
Via La Masa 1, 20156 Milano, Italy
E-mail: marco.mariani@polimi.it

F. Maspero
Department of Physics
Politecnico di Milano
Via Colombo 81, 20133 Milano, Italy

R. Bernasconi, L. Magagnin
Department of Chemistry, Materials and Chemical Engineering
i"Giulio Natta"
Politecnico di Milano
Via Mancinelli 7, 20131 Milano, Italy

make cobalt ferrite an ideal candidate for various technological applications, including magnetic storage media, microwave devices, magnetic sensors, and spintronics.[4–7] However, the successful deposition of cobalt ferrite films with controlled properties remains a challenge, and conventional deposition techniques often involve high-temperature processing, limiting the choice of compatible substrates and additional integration possibilities. Previous studies have proposed various manufacturing routes to achieve the reliable production of this material, as some of the following. Lee et al. explored the radio frequency magnetron sputtering process to produce films of several hundreds of nanometers and remarkable magnetic properties (3.9 kOe in the out-of-plane (OOP) direction), in correlation to the substrate and annealing temperature. Quickel et al. achieved a controlled mesoporous architecture by dip coating with an influence on the anisotropy of the material, thus revealing the possibility of achieving an anisotropic behavior through aligned porosity. Araujo et al. exploited laser ablation in a vacuum to produce patterns and underlined the importance of annealing to minimize the content of precursor oxides. Bagade and Rajpure produced thin films suitable for gas sensing by spray pyrolysis. Zhao et al. realized spin coating of a precursors-containing solution to produce 500 nm thick films by repeating the procedure eight times and featured remarkable coercivity (7.2 kOe) and large magnetic saturation, comparable to bulk hard magnets of this material.[8–12]

Traditional fabrication techniques for magnetic films, such as physical vapor deposition and sputtering, have proven successful in producing high-quality films.[12–14] However, these methods often suffer from limited scalability, high production costs, and complex equipment requirements. To overcome these challenges, additive manufacturing, including inkjet printing, has emerged as a promising alternative for the precise and efficient deposition of functional materials in many scientific and engineering fields: plastic electronics, flexible electronics, ceramic industry, sensor fabrication, and tissue engineering.[15–21]

Inkjet printing offers several distinct advantages over conventional fabrication methods.[22,23] First, it enables digital control of material deposition, allowing the creation of complex patterns with high resolution and spatial accuracy without the need for masks or etching. This level of precision is particularly beneficial

**ADVANCED
SCIENCE NEWS**

www.advancedsciencenews.com

**ADVANCED
ENGINEERING
MATERIALS**

www.aem-journal.com

for the design and development of miniaturized magnetic devices, such as microelectromechanical systems[24–26] and magnetic sensors.[11,27,28] Moreover, inkjet printing enables the use of a wide range of substrates, including flexible and nonplanar surfaces, expanding the potential applications of magnetic films to areas such as flexible electronics and wearable devices.

The inkjet printing of ferrites can be potentially carried out using both nanoparticle suspensions and sol-gel precursors. Both routes have been demonstrated in literature in the case of soft magnetic ferrites. Bissannagari et al. printed NiZn ferrite films using dispersions of $Ni_{0.4}Zn_{0.6}Fe_2O_4$ stabilized by BYK111.[29] Also, Hrakova et al. and Enuka et al. based their printing approach on the use of nanoparticles, specifically Ni–Mn–Zn ferrite nanoparticles.[30,31] On the contrary, sol-gel precursors were printed by Wu et al. for printing a bismuth ferrite and Kolchanov et al. for magnetite.[32,33] In this way, they successfully inkjet printed layers for nonvolatile resistive random-access memories. Regarding hard magnetic ferrites, virtually no literature is available. The only attempts to inkjet print a representative of this family of magnetic materials have been done by Son et al. and by Han et al.[34,35] The former provided extremely limited information about the final magnetic properties, while the latter printed lanthanum strontium cobalt ferrite layers to manufacture cathodes for high-performance solid oxide fuel cells. Consequently, even though lanthanum strontium cobalt ferrites are known to potentially have hard magnetic properties, these have never been measured in the case of inkjet-printed layers.[36] Considering the literature references discussed, it is evident that the inkjet printing of hard magnetic ferrites for magnetic applications, and in particular of cobalt ferrites, has never been investigated.

In this context, the present paper aims to explore a variety of strategies for the successful inkjet printing of cobalt ferrite films, including different printing systems, analysis of intermediate drying steps in multilayer depositions, annealing temperatures, and number of layers. This variety of printing and processing conditions provides a comprehensive description of the capabilities of the inkjet technique to deposit magnetic thick films with a remarkable temperature stability. A microstructural and magnetic characterization of the material obtained is presented as well and compared to the state of the art.

2. Results

2.1. Single Layer Deposition

The employment of the 10 pL cartridge in both printers allowed the repeatable and regular deposition of single droplets with an average diameter of 82 μm, as can be seen in **Figure 1**. Nevertheless, the formation of the initial layer with the Dimatix printer was critical. Indeed, the surface homogeneity was low, and it featured several unwetted spots, as well as material accumulation especially at the center of the film, regardless of the drop spacing. The concentrated ink prevents the risk of incomplete substrate wetting, but it does not entirely solve the "coffee stain" effect (light optical microscope (LOM) images in **Figure 2**).[37] These phenomena occur for the following reasons: 1) excessive droplet overlapping, especially for low drop spacings
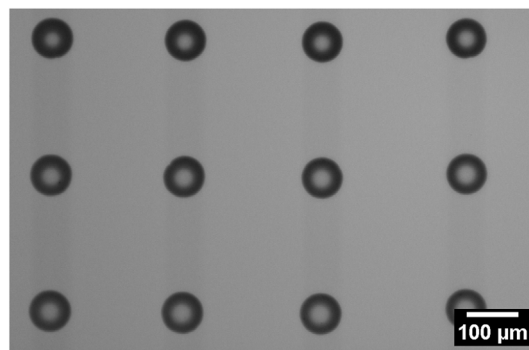

Figure 1. Test pattern with isolated droplets deposited by the 10 pL Fujifilm Dimatix cartridge in the Ceradrop printer.

(D1a); 2) insufficient wettability of the silicon substrate (D1b), which is improved by increasing the substrate temperature (D1c); and 3) absence of fast partial solvent evaporation after deposition due to the high evaporation point of DEG ($T_b = 250\,°C$).

The controlled overlapping of these droplets combined with a different deposition pattern (hexagonal) allows the formation of single layers granting a complete coverage of the substrate, as can be seen in the monolayer deposited by the Ceradrop printer (C1). Nonetheless, the coating homogeneity is still low, as can be observed from the appearance in the LOM image (Figure 2D). The dark spots are magnetization by an excessive accumulation of material due to the coalescence of the droplets prior to the evaporation of the ink solvents. This issue is further worsened during sintering because surface protrusions lead to formation of residual stresses in the film, resulting in macrocracks development. In addition, the density gradient generated by the presence of these clusters is responsible for different grain growth kinetics due to higher packing within the aggregate: as a result, grains are larger within the clusters with respect to the flat areas of the film surface (see image (A) of Figure S1, Supporting information).

All the vibrating sample magnetometer (VSM) loops (Figure 2) of sintered samples present a magnetic hysteresis, showing a hard behavior of the material. A clear distinction can be observed already for the monolayer sample treated at higher temperature (D1c), which shows a significantly larger coercivity and higher saturation magnetization with respect to the film sintered at low temperature (D1a, D1b, C1).

2.2. Multilayer Deposition

2.2.1. Interlayer Drying Strategies

The deposition of multiple layers (5 and 10 layers series), without specific interlayer drying procedures (Figure 4A), does not lead to resolution losses because successive layers are deposited on a porous surface that reduces droplet migration under the action of surface tension: excessive liquid motion and coalescence at the center of the square is limited. Still, the areas close to the boundaries of the films reveal a minor accumulation of materials, while
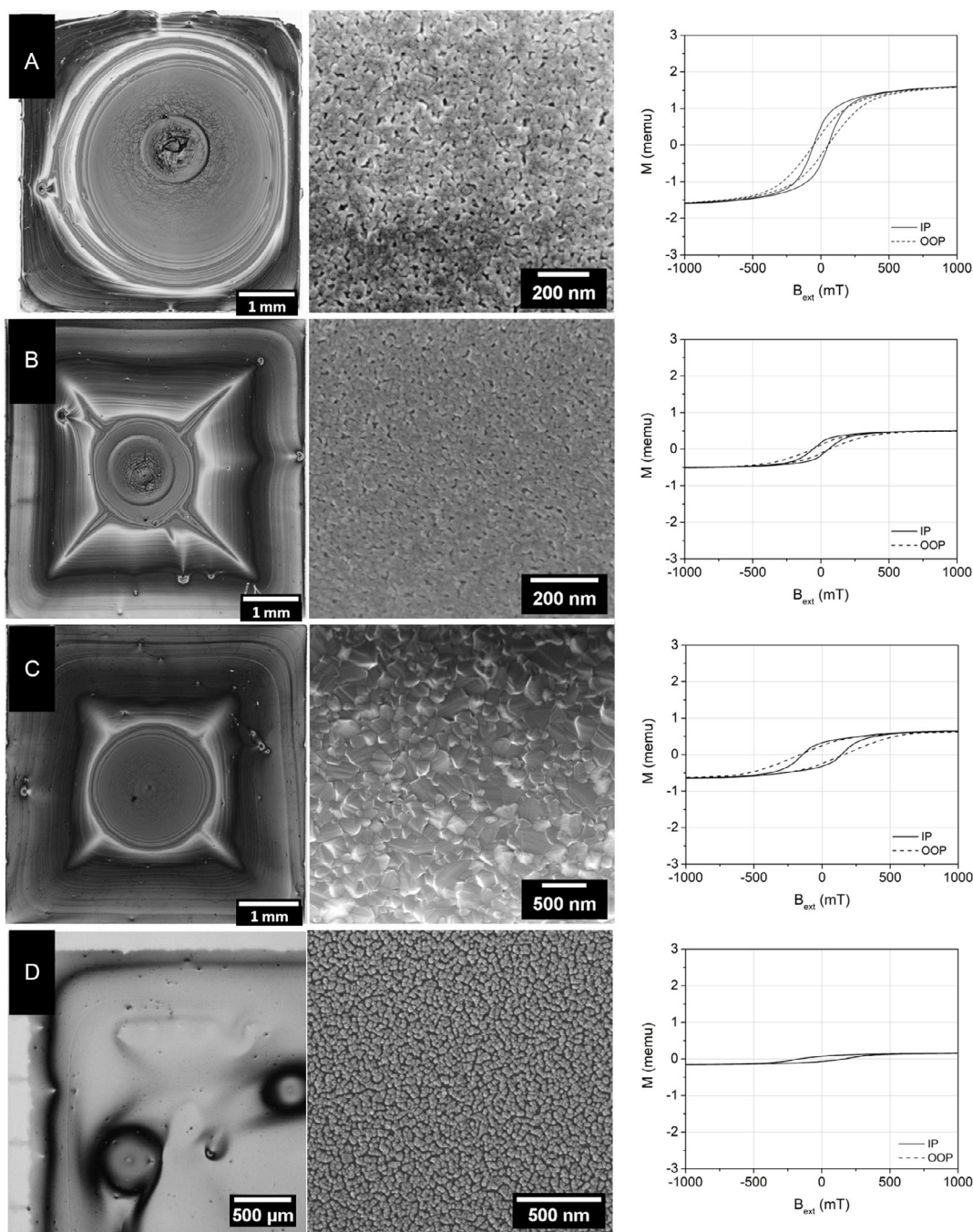
**ADVANCED
SCIENCE NEWS**

www.advancedsciencenews.com

**ADVANCED
ENGINEERING
MATERIALS**

www.aem-journal.com

Figure 2. Light optical microscope images (left), SEM micrographs (center), and vibrating sample magnetometer curves (right) of the monolayer samples: A) D1a, B) D1b, C) D1c deposited by the Dimatix printer, and D) C1 by the Ceradrop printer.

the center is partially affected by aggregation and microcracks formation due to the negligible evaporation of the solvent with a substrate temperature of 60 °C.

The exposure to infrared (IR) drying during multilayer depositions in the Ceradrop printer was also revealed to produce comparable roughness and inhomogeneity issues as the monolayer printed figures (see LOM images in Figure 4B,C). Instead, the interlayer drying by vacuum application allows to repeat a more regular deposition of several layers, as demonstrated by the appearance of linear patterns: the motion of liquid under surface tension is limited due to partial evaporation of the solvent; thus, particles remain aligned to the rasters. Profilometric characterizations (**Figure 3**) confirm the presence of discontinuous zones that lead to a very irregular surface and varying thicknesses, which could be progressively increased to about 120 and 260 nm with four and six layers, respectively. The deposition
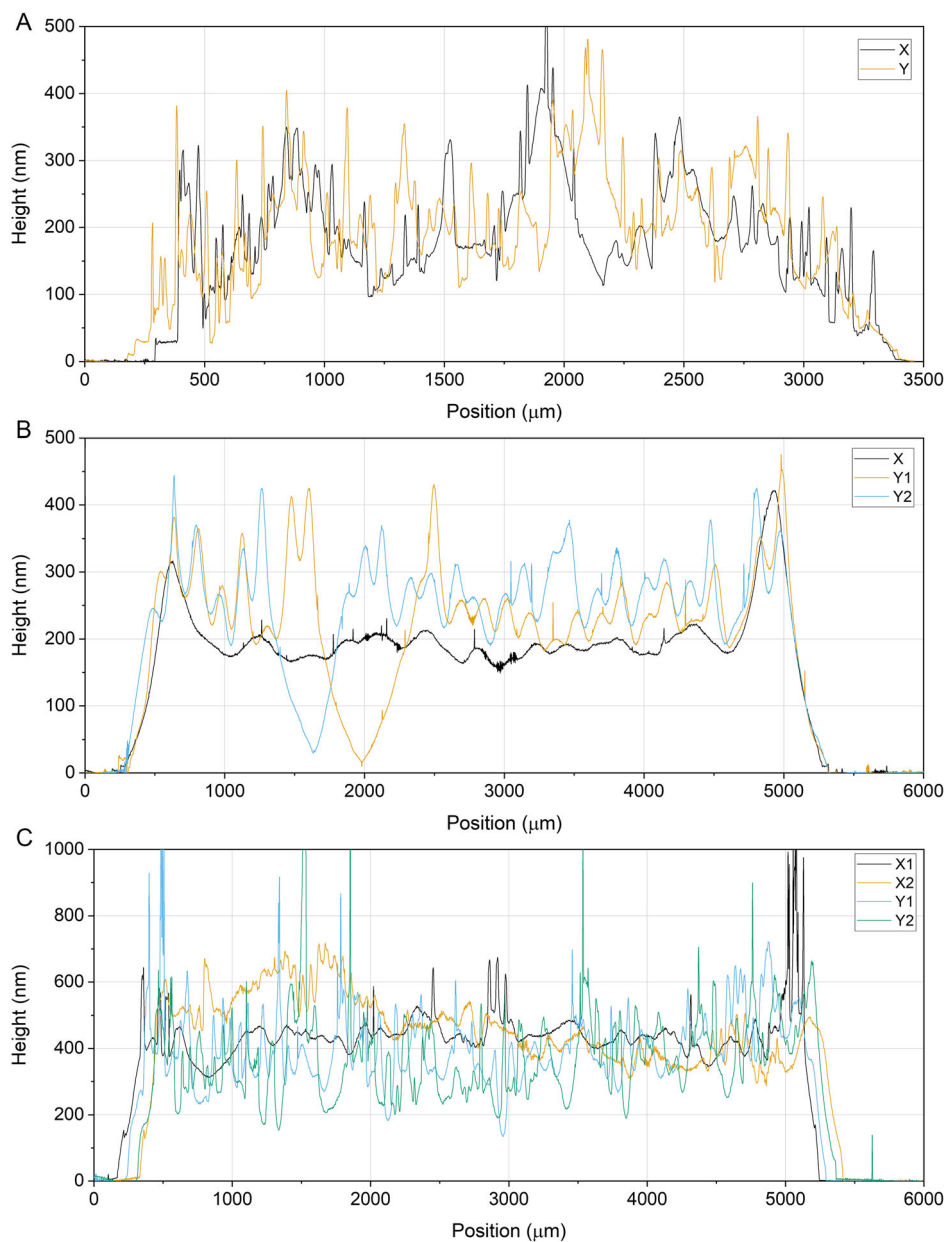
2400371 (3 of 13)

**ADVANCED
SCIENCE NEWS**

www.advancedsciencenews.com

**ADVANCED
ENGINEERING
MATERIALS**

www.aem-journal.com

Figure 3. Profilometric scans along (*x*) and across (*y*) the printing axis of the surface of the A) C4a, B) C6c, and C) C14 samples.

of several layers in sample C14 demonstrated that the material remains preferentially distributed along rasters, but there are no unwetted spots, and the average film thickness is about 340 nm. In addition, the use of vacuum does not affect the substrate temperature, which, on the contrary, was heated above 70 °C with the use of the IR lamp.

The use of the concentrated ink was possible already with the cartridge dispensing 10 pL droplets, but it was strictly required with those featuring 1 pL droplets, since in this case, the diluted ink did not result in correctly generated droplets without issues such as satellites formation. This new combination did not completely avoid the homogeneity problems: the three white spots visible in the upper region of the film in **Figure** 4F are

unwetted areas, which correspond to valleys in the thickness profiles (see Y1 and Y2 lines in Figure 3B). Nevertheless, profilometric analyses (Figure 3) show reduced surface waviness and inhomogeneities, with an average thickness of 220 nm for six layers, in films produced with the concentrated ink. The detected profile across the rasters (*y*-axis) displays a periodicity in the presence of valleys and peaks, while the waviness depth is less pronounced in the parallel direction (*x*-axis). In addition, the scan along the *x*-axis shows that there is an accumulation of material at the borders of the film. Such defect is well-known as "coffee stain effect": a migration of material to the edges of the printed area occurs while drying, as a result of the surface tension acting on the liquid surface.
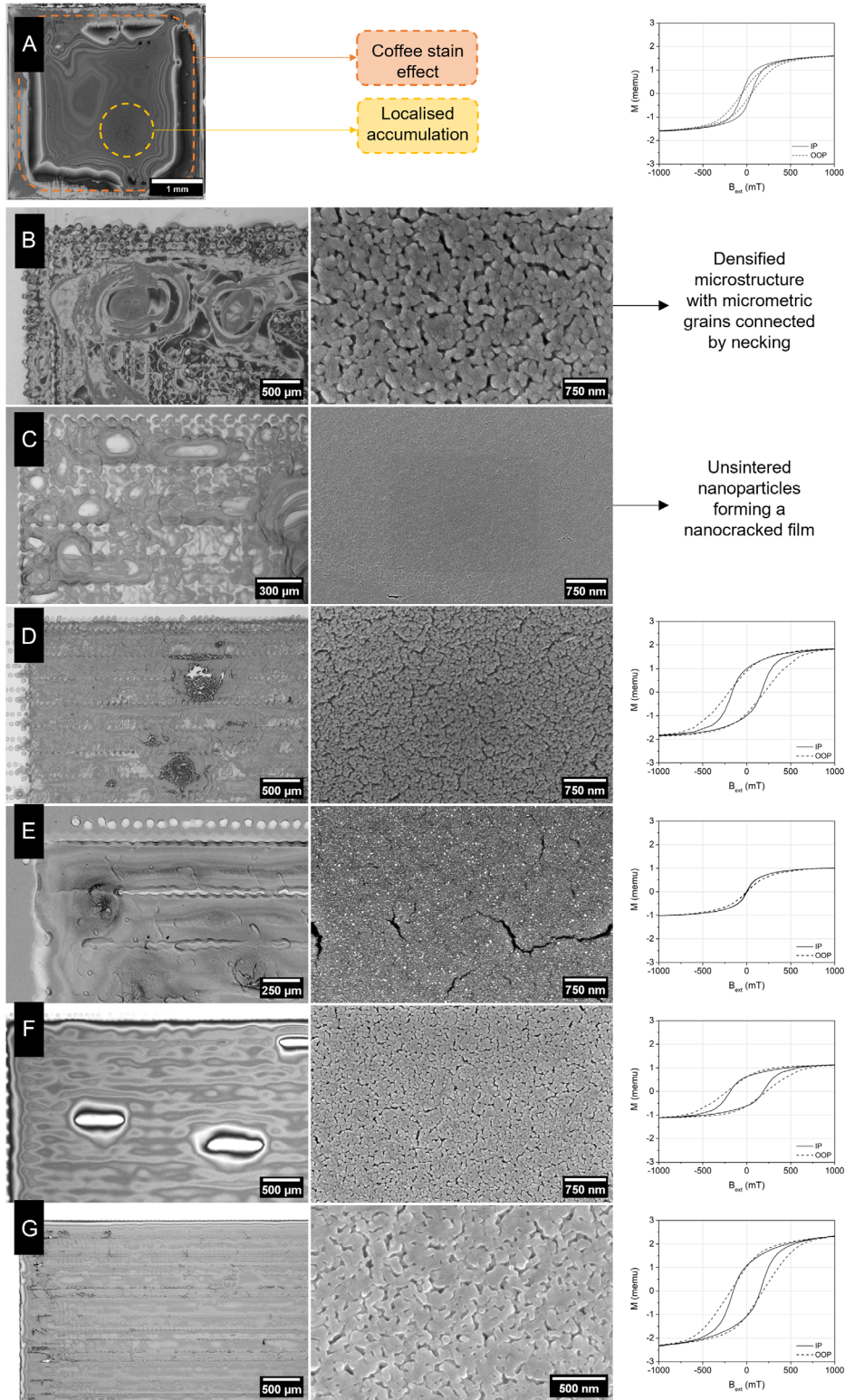
2400371 (4 of 13)

Figure 4. Light optical microscope images (left), SEM micrographs (center), and vibrating sample magnetometer curves (right) of the following samples: A) D5a, B) C4a, C) C4b, D) C6a, E) C6b, F) C6c, and G) C14.

2.2.2. Effects of Sintering on Microstructural and Functional Properties

Scanning electrode microscope (SEM) analyses on the surface of multilayer samples after sintering reveal microstructures constituted by evenly distributed nanometric grains contacted by necking. Up to 800 °C densification is not completed; thus, residual porosity can be observed in all cases, likely due to insufficient material accumulation and to the competitive coarsening mechanism that tends to promote grain coarsening rather than eliminate porosities (see SEM micrographs in Figure 4B,D,F,G).

Multilayer printing on polyimide (PI) substrates is feasible without varying the deposition parameters, but samples present an extensively cracked surface with widespread nanocracks (see image (B) of Figure S1, Supporting information). Those defects likely generate during debinding due to a series of potential issues: 1) different thermal expansion coefficients of Si and PI that may promote distortions of the polymeric substrate; 2) aggregation of deposited particles; 3) formation of free paths for gas removal during debinding; and 4) a combination of the previous cases.

Nanocracks are not observed in sintered samples onto Si: these are likely closed due to film shrinkage during densification. The absence of any densification of particles at the debinding temperature applied for films on PI is confirmed by the magnetic behavior observed for C6b (Figure 4E): it is superparamagnetic with moderate saturation magnetization values and low coercivity, typical of isolated nanoparticles.[13,38] Such a result is coherent with the size of the nanoparticles in the ink that is below 10 nm, thus close to the superparamagnetic limit corresponding to 6 nm. Results show that magnetic properties become slightly anisotropic with the increase of the number of deposited layers, leading to mismatching values of a coercive field in dependence on the direction of the applied field: in all cases, the OOP value is equal or higher than the in-plane (IP) one.

At sintering temperatures from 800 to 950 °C, the film's microstructure features residual porosity. The grain size is similar, although progressive coalescence can be clearly observed, as shown in SEM images from **Figure 5** and quantified in **Figure 6**.[8] Samples treated at least at 950 °C display twinned grains, whose growth follows the typical arrangement of spinel structure onto the {111} octahedral planes, and average grain sizes exceed 70 nm. For densification at 1000 °C (D10e), the surface looks almost free from pores, and the microstructure changes significantly: the average grain size reduces as a consequence of the nucleation of new grains with dimensions below 20 nm. These seem to have in most cases a simple octahedral morphology, and they might result from the nucleation of twinned boundaries on all free {111} planes of the main grains.[39]

Hereafter, the X-ray diffractometer (XRD) characterizations of the five sintered multilayer samples are reported in **Figure 7**. The CFO main peak is the (311) plane, identified in all cases in correspondence of 2θ close to 35.4°. This position is comparable to the diffraction peaks produced by $(Co_{0.255}Fe_{0.745})(Co_{0.745}Fe_{1.255})O_4$ (COD ID number: 1533163): cobalt and ferrite cations are present at tetrahedral and octahedral sites; thus, the spinel structure is mixed and not perfectly inverse. It must be noted that the

exposure to high temperatures allows the formation of a series of secondary phases with varying degrees of content of cobalt, iron, and silicon. Indeed, it can be observed the presence of multiple secondary peaks associated with the silicothermic reduction of compounds, thus obtaining: 1) the substitution of Co^{2+} cations with Si^{4+} to form the spinel $Si_xFe_{3-x}O_4$, with an orthorhombic lattice, or Fe^{2+} to form Fe_3O_4 magnetite (its characteristic peaks are not visible due to overlap with CFO and Si diffraction patterns);[40] and 2) the transformation into $SiCo_2O_4$ (olivine-type structure) with Fe^{3+} and Si^{4+} cations substituting Co^{2+}.

The occurrence of these mechanisms is promoted by the relatively open spinel structure with a large fraction of unoccupied interstitial sites.

The onset of secondary phase formation promoted during annealing is confirmed by energy-dispersive X-ray spectroscopy (EDX) analyses as well. Indeed, surface-averaged measurements of the elemental composition of monolayer and multilayer samples revealed the presence of a non-negligible amount of silicon in addition to cobalt, iron, and oxygen. EDX analyses (Figure 7, **Table 1**) on areas of samples obtained from different sintering temperatures reveal that the proportion of Co:Fe:O = 1:2:4 is maintained, thus confirming that CFO is the main phase in all cases.[41] The signal correlated to silicon is strong in the D10a sample, but it is impossible to determine the fraction of the radiation generated by the silicon substrate from that originating from silicon oxides in the films.

The analysis of the main diffraction peak (311) of CFO reveals that crystallite (d) size, as well as grain size, grows with the temperature up to 950 °C, and then they are subjected to a reduction.[3] It can be observed that sintering below 850 °C produces a limited grain growth (avg. grain size <35 nm) and retains d close to or below the single-domain limit of 28 nm. A reduction of the crystallite size is observed again for D10e, likely due to the influence of the nucleated grains after recrystallization.

The ratio among the intensities of the peaks associated with the (220) and (222) planes varies as well. A minimum is observed for D10b, and then the value increases almost linearly up to 3.25.[42] Such behavior is consistent with the progressive transition from a mixed spinel of the original powder (low $I_{(220)}/I_{(222)}$) to a more ordered inverse spinel (high $I_{(220)}/I_{(222)}$) promoted by higher annealing temperatures.

Regarding the 10 layers films in the IP configuration, coercivity rises until 950 °C, whereas it decreases when passing from 950 to 1000 °C; however, this trend is not observed for the OOP configuration where the minimum is registered for D10d (Figure 9). This sample also provides the largest difference of squareness among the IP and OOP cases, with the latter being much lower. All squareness ratios have values below the 0.5 threshold, which is the theoretical limit for a randomly oriented uniaxial system; thus, the material should not feature a cubic anisotropy, whose theoretical limit is 0.83.[43] It should also be noted that in both directions, the saturation magnetization features a minimum in correspondence of D10c and maximum values after sintering at 800 and 1000 °C. The discrepancy among the values in the IP and OOP directions suggests that the material features a magnetic anisotropy owing to the aspect ratio[44] and due to stress accumulation during sintering at the CFO/Si interface.[12]
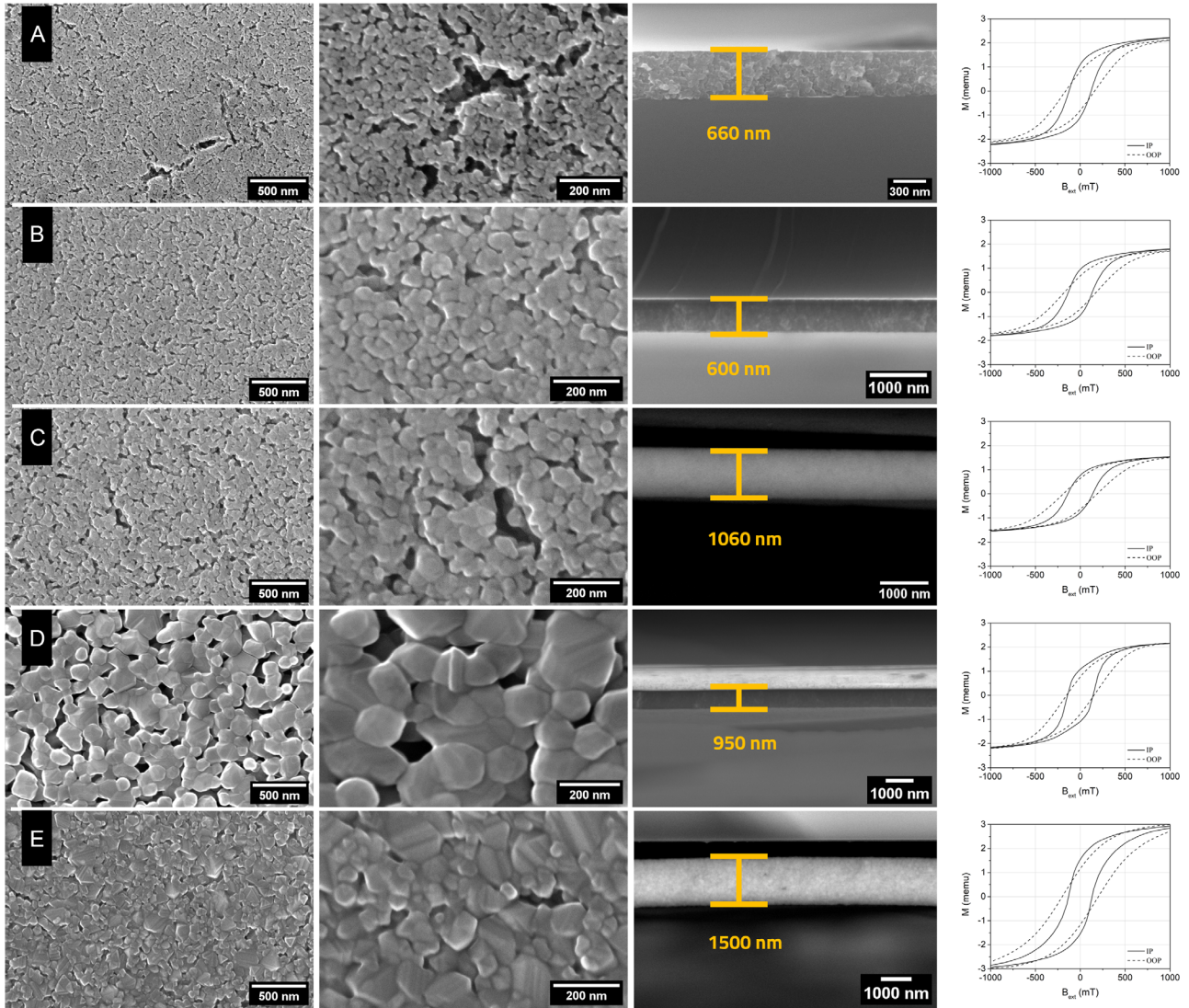
Figure 5. SEM images of the surfaces (left) and the cross sections (center) at different magnifications and vibrating sample magnetometer graphs (right) of samples densified at increasing temperatures from 800 to 1000 °C, identified as A) D10a, B) D10b, C) D10c, D) D10d, and E) D10e.
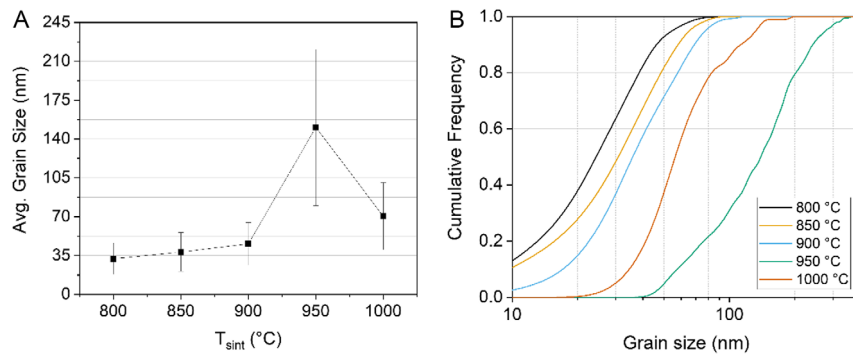

Figure 6. A) Average grain size and B) grain size distribution curves of the D-10L series sintered at temperatures from 800 to 1000 °C.
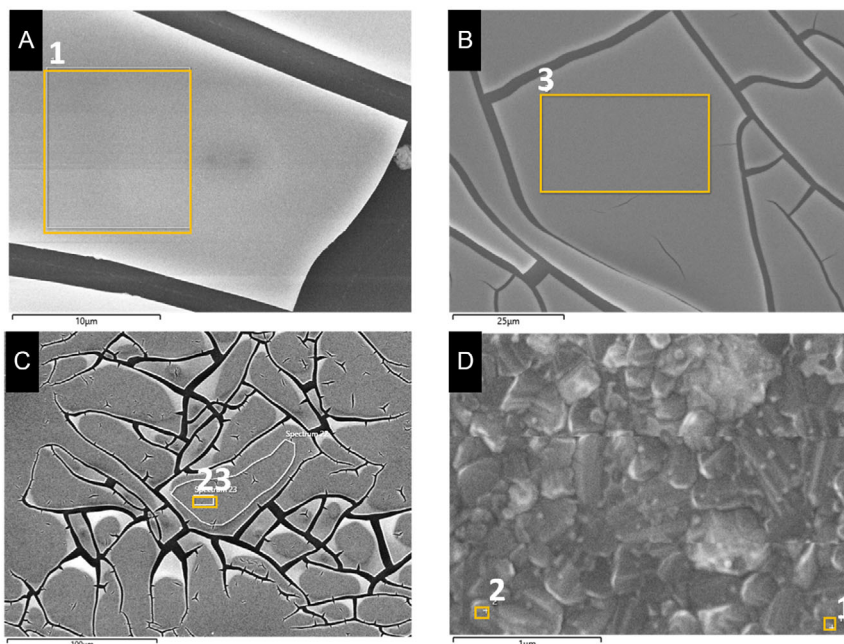
Figure 7. Images of the scanned areas for the EDX analyses from A,B) D1b, C) D10a, and D) D10e samples.

Table 1. Elemental concentrations (at%) measured in the areas highlighted in Figure 7.

Sample	Spectrum	O [at%]	Fe [at%]	Co [at%]	Si [at%]
D1b	1	54.6	28.7	14.3	2.5
	3	53.6	23.1	12.0	11.2
D10a	23	50.5	23.0	10.4	16.1
D10e	1	55.7	29.8	13.6	0.9
	2	56.7	28.9	14.0	0.4

3. Discussion

3.1. Printing Strategy

The morphology and the microstructure of the deposited films are strictly dependent on the printing parameters and the thermal treatment applied.

The ink rheology can be controlled by modifying the solid loading and/or introducing additives in the suspension, thus achieving a proper droplet formation. Nonetheless, the volume of particles deposited is generally inferior to that of the liquid; thus, there is the need of partially overlapping droplets on the substrate to obtain a complete coverage of the printed area. In our case, an optimization of the droplet spacing or a different patterning strategy (hexagonal lattice deposition) allowed us to minimize the low homogeneity of the single layers, although the typical "coffee stain" effect remains visible (Figure 2C,D). Subsequent layers benefit from the porosity/rugosity of the previously deposited surfaces, thus featuring a limited mobility of the droplets under the effect of surface tension. A specific interlayer drying strategy is required in our case: diethylene glycol (DEG) prevents the quick evaporation of the droplet due to substrate heating or exposure to infrared IR radiation, while the application of vacuum seems to be effective in rapidly reducing the volume of liquid and fixing the deposited particles on their landing site.

Finally, the sintering temperature is responsible for the degree of densification and grain growth. Lower temperatures allow a more predictable development of the feedstock particles into partially densified grains connected by necking, while high temperatures grant a complete closure of the film porosity. These competitive mechanisms feature a sharp change in behavior between 950 and 1000 °C owing to the twinning of enlarged grains and recrystallization at the surfaces and boundaries of the preexisting grains. In addition, the temperature is responsible for the development of the spinel structure of the main phase, while secondary phases are not significantly affected.

3.2. Magnetic Properties

The magnetic behavior is dependent on a series of factors: 1) the crystallite size d with respect to the single-domain limit; 2) the degree of inversion of the spinel lattice (positively correlated to $I_{(220)}/I_{(222)}$, see **Figure 8**); and 3) the extension of the grain boundaries (GB), thus the grain size, and the surface area of the pores, that is, the rate of densification.

Up to a sintering temperature of 850 °C, coercivity slightly increased, and magnetic saturation is decreased both in the IP and OOP directions (**Figure 9**). These samples are characterized by a progressively larger grain size, a decreasing degree of spinel
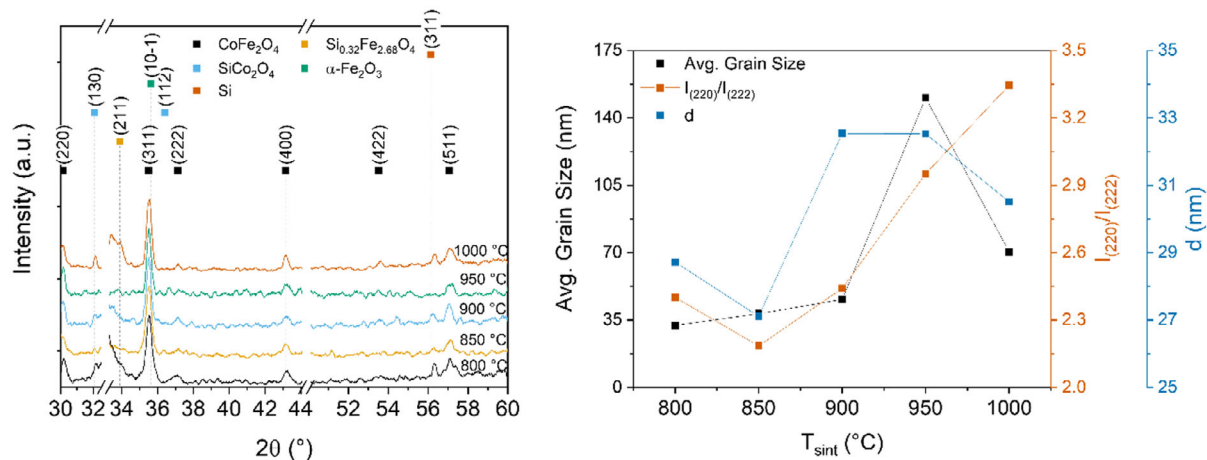
Figure 8. X-ray diffractometry curves (COD ID numbers: $CoFe_2O_4$ – 1533163, $Si_xFe_{3-x}O_4$ – 9001421, $SiCo_2O_4$ – 9001069, Fe_2O_3 – 1011240) and calculated parameters ($I_{(220)}/I_{(222)}$ and crystallite size d) of the D-10L series sintered at temperatures from 800 to 1000 °C.
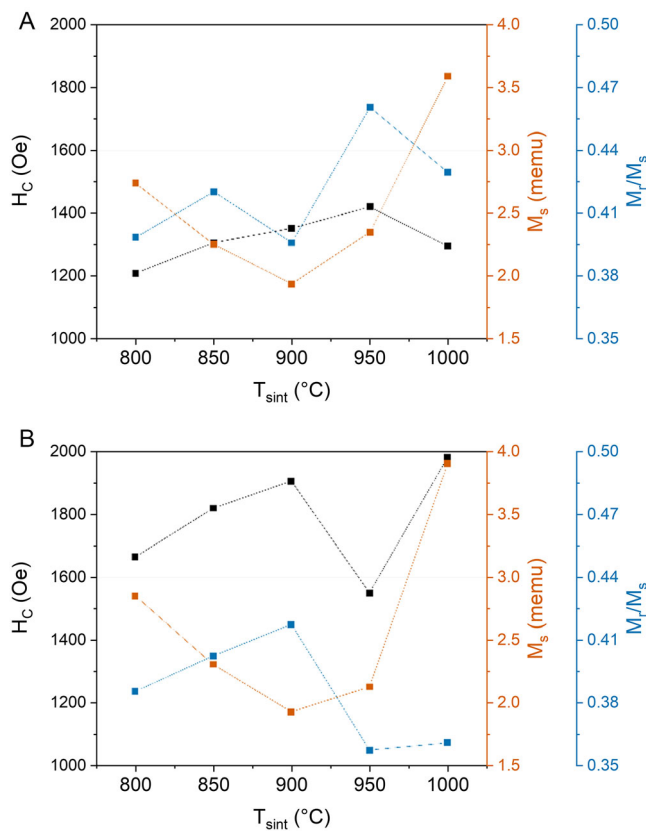

Figure 9. Coercivity (H_C), saturation magnetization (M_S), and squareness (M_R/M_S) values for the sintered samples of the D-10L series in A) the IP and B) the OOP directions.

inversion, and comparable crystallite sizes (Figure 8). A fewer extension of the GB (i.e., larger grains) should be beneficial to M_S and detrimental to H_C; thus, grain size and densification are not the dominant factors at this stage, as demonstrated by Mohaideen et al.[45] The reduction of the inversion degree should

have the same effect; therefore, the variation in properties must primarily be dependent on the crystallite size, which was below the single-domain limit only for D10b. Such a strict dependence on the coercive field of cobalt ferrite was observed by Maaz et al. as well.[46]

After sintering at 900 °C, the trends are maintained for all parameters except for the squareness in the IP configuration, due to the decrease of M_R. At this stage, the only relevant variation is the growth of the crystallite size, which moves clearly in the multi-domain field.

D10d displays an increase in the coercivity and saturation magnetization, thus a reduction of squareness, in the IP direction. Both coercivity and squareness are lower for the OOP configuration. With respect to D10c, the crystallite size is stable, but the grain size and the degree of inversion of the spinel structure increase considerably. The consistent reduction of the grain boundary regions justifies the increase of the saturation value, while the formation of a more ordered inverted structure prevents the reduction of H_C.[47,48] The fact that this behavior is not repeated in the OOP direction suggests that the observed grain growth is not isotropic but possibly favored along the planar direction in correspondence with the deposited layers with residual porosity preferentially distributed among them.

Finally, D10e shows a drastic increase in M_S with respect to all previous samples, while squareness and coercivity are similar to D10c, especially in the IP direction (Figure 9). The microstructure reveals the concurrent presence of enlarged grains and newly nucleated ones (Figure 5). The latter is responsible for the reduction of the average crystallite size and pores surface. The spinel structure is further inverted thanks to the higher thermal energy provided. This, combined with the presence of small grains featuring a single-domain behavior, justifies the decent coercivity. Nonetheless, the saturation value is improved by the enlarged grains and possibly the higher densification of the film.[2,29] The increase of M_S and the concurrent decrease of the coercive field exclude the possibility of a significant effect of secondary phases generated by Si ions substitutions on the magnetic properties.[49]

**ADVANCED
SCIENCE NEWS**

www.advancedsciencenews.com

**ADVANCED
ENGINEERING
MATERIALS**

www.aem-journal.com

4. Conclusion

The study proves the feasibility of inkjet printing of magnetic patterns (**Figure 10**) of cobalt ferrite. Different aspects of the manufacturing and processing procedure are considered, and their effects are assessed through microstructural and magnetic characterization. It was observed that: 1) Stable colloidal suspension of nanometric ferrite particles could be modified and employed to form regular droplets by printhead cartridges with varying nozzle sizes, thus granting the possibility of adapting the same feedstock to different manufacturers; 2) Single and multiple layer depositions were obtained without resolution losses thanks to intermediate drying procedures that prevented out-of-pattern wetting. This led to the production of a wide range of films with varying thicknesses and magnetic properties after sintering; 3) Sintering treatments at high temperatures (>500 °C) were revealed to be necessary to obtain a hard ferro- or ferrimagnetic behavior. Nonetheless, as-printed or debinded films could be employed for applications where superparamagnetic properties are needed; 4) Sintering led to progressive grain coarsening up to 950 °C, followed by twinning, nucleation of finer grains at the grain boundaries, and densification at 1000 °C; 5) Regardless of the printing and sintering procedures, the films featured a low surface regularity due to high roughness, direction of rasters, incomplete wetting of the printed areas, and coalescence of droplets prior to solvent evaporation; 6) The maximum coercivity value obtained was equal to ≈2 kOe in the IP and OOP directions by films sintered at 1000 °C, thus confirming that porosity reduction and nucleation of fine grains with size close to the single-domain limit are beneficial; and 7) Maximization of the saturation magnetization was obtained by sintering at high temperature (1000 °C), thanks to minimization of surface effects, or low temperature (800 °C), owing to the limited growth of grains and domains.

These findings demonstrate the potential of inkjet printing for the fabrication of magnetic films with complex patterns.

5. Experimental Section

Ink Preparation and Properties: A well-dispersed suspension of cobalt ferrite ($CoFe_2O_4$ – CFO) nanoparticles in DEG was employed as the starting material. This suspension was developed by CNR-ISSMC (Faenza, Italy) and Ce.Ri.Col. (Colorobbia Research Center, Empoli, Italy) from a modified polyol process, and it features a solid fraction equal to 3 wt%; the production process and the ink properties are described in previous works.[50–53] In brief, the particles are obtained by in situ synthesis from metal precursors in the organic medium (glycol) heated above 150 °C, which allows to control their growth and simplify their stabilization in the solvent.[54]

The particle shape and initial size were characterized by a Philips CM 200 transmission electron microscope confirming a mean particle size of 5–6 nm with a spherical shape (**Figure 11**A). In addition, XRD analysis (SmartLab SE Rigaku) was conducted on the dried powder to identify the phases (main phase: $CoFe_2O_4$; secondary phase: Fe_2O_3), using a Cu-Kα incident radiation ($\lambda = 1.5406$ Å), demonstrating the high purity of the solid fraction in the suspension (Figure 11). The $I_{(220)}/I_{(222)}$ calculated from the graph is equal to 1.96.

A second ink was obtained by concentrating the initial suspension to 5.36 wt%. through partial evaporation of DEG in a rounded flask. Commercially available dispersants DISPERBYK-145 and DISPERBYK-110 (BYK-Chemie GmbH, Wesel, Germany) were added at the total concentration of 0.1 wt% with respect to the CFO fraction to prevent sedimentation and aggregation during the evaporation. The second concentrated

Figure 10. Logo of Politecnico di Milano printed by deposition of the concentrated cobalt ferrite ink on silicon by the Dimatix 3D printer.
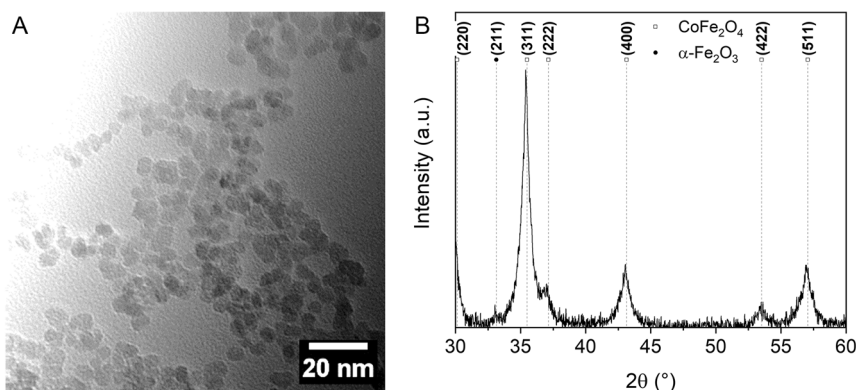

Figure 11. Transmission electron microscope image (A) and X-ray diffractometry spectrum of the dried powder from the ink.

suspension was prepared to provide a higher loading of particles on the printed substrate after debinding and ease the process of densification of the deposited material. The surface tension of the ink was measured by the du Nouy ring method with Zuidema correction, resulting in 42.73 mN m^{-1}.

Finally, a third ink was developed starting from the concentrated one by adding water: the final solid loading was 4.25 wt%, and the DEG/water ratio was 4:1.

Film Deposition: The inks were deposited on Si substrates or PI-coated substrates. The former underwent the following cleaning and activation treatments: 5 min of ultrasonic bath in acetone, followed (if necessary) by 3 min of ultrasonic bath in isopropanol, both carried out at 59 kHz, and then an O$_2$ plasma treatment for 3 min at 400 W and 1 mbar. The latter underwent the following cleaning and activation treatments: 5 min of ultrasonic bath in acetone, followed by 3 min of ultrasonic bath in isopropanol, both carried out at 59 kHz, and finally, an O$_2$ plasma treatment for 2 min at 120 W and 1 mbar. In order not to lose the improved wettability, the substrates were cleaned just prior to printing, after the tuning of the printing parameters and cartridge loading.

Two inkjet printers were employed to determine the printability of the suspension and to study different strategies of deposition.

One batch of films was printed by a Ceradrop F-Serie printer (CERADROP, Limoges, France) equipped with Fujifilm Dimatix cartridges able to dispense either 10 or 1 pL droplets. In the first case (10 pL), the diluted suspension (3 wt%) was employed, while the concentrated ink (5.4 wt%) was strictly necessary with the second cartridge (1 pL) to obtain a stable droplet formation. Then, different types of films were produced by the deposition of one or more layers with a hexagonal lattice pattern with 38% drop overlapping and nozzle temperature of 45 °C, identified as the more suited condition in the typical printability region of piezoelectric printheads. The samples deposited on Si were thermally treated to debind and sinter in a single cycle: 280 °C, 30 min, 5 °C min^{-1} + 800 °C, 30 min, and 5 °C min^{-1}. Those deposited on PI were only debinded at 250 °C for 30 min to prevent the degradation of the substrate. In case of multilayers depositions, interlayer drying procedure were achieved either by exposure to an IR lamp or by the application of low vacuum ($\approx$2 mbar) for 3 min.

The second batch of samples was printed through a Fujifilm Dimatix Materials DMP-2850 printer (FUJIFILM Corporation, Tokyo, Japan) equipped with a cartridge for 10 pL drop volume. The nozzle temperature was kept fixed at 45 °C, while different combinations of drop spacings in a square pattern, substrate temperature, and number of layers were tested to understand the effect of each factor on the formation of the films and potential defects. In this case, debinding was performed through multiple steps since there were no drying stages during printing. The debinding temperature was set at 250 °C for 30 min with a 2 °C min^{-1} ramp, with the following holding steps to prevent the onset of thermal stress during cooling: 150 °C for 10 min and 200 °C for 10 min. Sintering was carried out with a 4 °C min^{-1} ramp to different selected temperatures for each sample. The summary of the printing conditions is reported in **Table 2**.

Film Characterization: The surface of the sintered films was studied to determine the rate of densification and grain growth, while cross sections were analyzed to determine the thickness of the printed samples. Microstructures were observed through a Nikon Eclipse LV150NL LOM and a Zeiss Sigma 500 VP field emission SEM. The grain sizes of the sintered samples were determined from the SEM images by automatic detection, starting from a minimum of 10 nm through the Trainable WEKA Segmentation plugin of the ImageJ software. The distribution frequency curves were calculated using a binning of 10 nm, with minimum and maximum sizes of 5 and 400 nm, respectively.

The printed patterns were characterized by contact profilometry with a diamond stylus-equipped profilometer (KLA Tencor P-17) to provide thickness and roughness values. The linear profile was evaluated both in the parallel (*x*) and perpendicular (*y*) directions with respect to that of the rasters and in specific areas to evaluate the extent of defects in the thickness of the film.

As-printed and sintered films were magnetically characterized with the MicroSense VSM EZ-9 by applying an external magnetic field from -2 to $+2$ T both for the IP and the OOP configurations. The VSM is calibrated using a NiFe bulk sample of known magnetic moment having the same area as the CoFeB sample. The calibration is performed for IP configuration, while a correction coefficient is applied to OOP curves to obtain the same saturation magnetization of IP measurements (CoFeB saturates before 2 T; therefore, saturations should match). The diamagnetic contribution of the substrate is subtracted by fitting the saturated region of the hysteresis curve. This procedure should give a quantitative value of the magnetization of the sample; however, the measured values normalized by the volume of the sample can only provide a qualitative description of the magnetic behavior of the films: the coatings thickness was not homogeneous; therefore, mediated values obtained from SEM and profilometry were considered as constant for all the analyzed sections.

Table 2. Summary of the printing conditions.

Sample	Ink loading [wt%]	Drop volume [pL]	Substrate [Type]-[°C]	Layers	Drop spacing [μm]	Drying	$T_{\text{sintering}}$ [°C]
C1	3	10	Si − 50	1	−	−	800
C4a	3	10	Si − 50	4	−	IR	800
C4b	3	10	PI − 50	4	−	IR	−
C6a	3	10	Si − 50	6	−	LV	800
C6b	3	10	PI − 50	6	−	LV	−
C6c	5.4	1	Si − 50	6	−	LV	800
C14	5.4	1	Si − 50	14	−	LV	800
D1a	4.3	10	Si − 45	1	20	−	600
D1b	4.3	10	Si − 50	1	40	−	700
D1c	4.3	10	Si − 60	1	40	−	1000
D5a	4.3	10	Si − 60	5	60	−	600
D10a	4.3	10	Si − 60	10	60	−	800
D10b	4.3	10	Si − 60	10	60	−	850
D10c	4.3	10	Si − 60	10	60	−	900
D10d	4.3	10	Si − 60	10	60	−	900
D10e	4.3	10	Si − 60	10	60	−	1000

**ADVANCED
SCIENCE NEWS**

www.advancedsciencenews.com

**ADVANCED
ENGINEERING
MATERIALS**

www.aem-journal.com

Phase identification on sintered materials was carried out by means of XRD with a Rigaku SmartLab XE. The crystallite size d was calculated by employing the Scherrer equation. The diffractograms feature breaks at $32.7° < 2\theta < 33.2°$ and $44° < 2\theta < 50°$ to eliminate the substrate main peaks, as the basis-forbidden Si (200) reflection, which can be several orders of magnitude larger than the film signal.[55]

Supporting Information

Supporting Information is available from the Wiley Online Library or from the author.

Conflict of Interest

The authors declare no conflict of interest.

Data Availability Statement

The data that support the findings of this study are available from the corresponding author upon reasonable request.

[1] A. López-Ortega, E. Lottini, C. de Julián Fernández, C. Sangregorio, *Chem. Mater.* **2015**, *27*, 4048.

[2] N. A. M. Pauzi, R. Nazlan, N. M. K. Anuar, M. A. Jusoh, I. R. Ibrahim, F. N. Shafiee, *Mater. Today Proc.* **2022**, *51*, 1420.

[3] S. I. Ahmad, *J. Magn. Magn. Mater.* **2022**, *562*, 169840.

[4] P. C. Fannin, C. N. Marin, I. Malaescu, N. Stefu, P. Vlazan, S. Novaconi, P. Sfirloaga, S. Popescu, C. Couper, *Mater. Des.* **2011**, *32*, 1600.

[5] P. N. Anantharamaiah, H. M. Shashanka, S. Saha, J. A. Chelvane, B. Sahoo, *J. Alloys Compd.* **2021**, *877*, 160285.

[6] M. Tanaka, M. Furuta, T. Ichikawa, M. Morishita, Y.-M. Hung, S. Honda, T. Ono, K. Mibu, *Appl. Phys. Lett.* **2023**, *122*, 042401.

[7] P. Chen, Y.-Y. Huang, G. Bhave, K. Hoshino, X. Zhang, *Ann. Biomed. Eng.* **2016**, *44*, 1710.

[8] J.-G. Lee, K. P. Chae, J. C. Sur, *J. Magn. Magn. Mater.* **2003**, *267*, 161.

[9] T. E. Quickel, V. H. Le, T. Brezesinski, S. H. Tolbert, *Nano Lett.* **2010**, *10*, 2982.

[10] C. Araújo, B. G. Almeida, M. Aguiar, J. A. Mendes, *Vacuum* **2008**, *82*, 1437.

[11] A. A. Bagade, K. Y. Rajpure, *J. Alloys Compd.* **2016**, *657*, 414.

[12] C. Zhao, A. Gao, Y. Yang, C. Tu, A. Bhutani, K. A. Walsh, S. Gong, D. P. Shoemaker, *AIP Adv.* **2019**, *9*, 035126.

[13] J.-G. Lee, H. M. Lee, C. Sung Kim, O. Young-Jei, *J. Magn. Magn. Mater.* **1998**, *177–181*, 900.

[14] R. Bachelet, P. de Coux, B. Warot-Fonrose, V. Skumryev, J. Fontcuberta, F. Sánchez, *Thin Solid Films* **2011**, *519*, 5726.

[15] H. Sirringhaus, T. Kawase, R. H. Friend, T. Shimoda, M. Inbasekaran, W. Wu, E. P. Woo, *Science* **2000**, *290*, 2123.

[16] S. G. Kirtania, M. A. Riheen, S. U. Kim, K. Sekhar, A. Wisniewska, P. K. Sekhar, *Micromachines* **2020**, *11*, 841.

[17] K. A. M. Seerden, N. Reis, J. R. G. Evans, P. S. Grant, J. W. Halloran, B. Derby, *J. Am. Ceram. Soc.* **2001**, *84*, 2514.

[18] L. Setti, A. Fraleoni-Morgera, B. Ballarin, A. Filippini, D. Frascaro, C. Piana, *Biosens. Bioelectron.* **2005**, *20*, 2019.

[19] M. Nakamura, A. Kobayashi, F. Takagi, A. Watanabe, Y. Hiruma, K. Ohuchi, Y. Iwasaki, M. Horie, I. Morita, S. Takatani, *Tissue Eng.* **2005**, *11*, 1658.

[20] C. Zhang, X. Li, L. Jiang, D. Tang, H. Xu, P. Zhao, J. Fu, Q. Zhou, Y. Chen, *Adv. Funct. Mater.* **2021**, *31*, 2102777.

[21] K. J. Merazzo, A. C. Lima, M. Rincón-Iglesias, L. C. Fernandes, N. Pereira, S. Lanceros-Mendez, P. Martins, *Mater. Horizons* **2021**, *8*, 2654.

[22] M. Singh, H. M. Haverinen, P. Dhagat, G. E. Jabbour, *Adv. Mater.* **2010**, *22*, 673.

[23] M. Vaseem, F. A. Ghaffar, M. F. Farooqui, A. Shamim, *Adv. Mater. Technol.* **2018**, *3*, 1870013.

[24] R. Bernasconi, G. Pietro Invernizzi, E. Gallo Stampino, R. Gotti, D. Gatti, L. Magagnin, *Micromachines* **2023**, *14*, 2082.

[25] N. Jackson, F. J. Pedrosa, A. Bollero, A. Mathewson, O. Z. Olszewski, *J. Microelectromech. Syst.* **2016**, *25*, 716.

[26] F. Niekiel, J. Su, M. T. Bodduluri, T. Lisec, L. Blohm, I. Pieper, B. Wagner, F. Lofink, *Sens. Actuators, A* **2019**, *297*, 111560.

[27] X. Liu, T. J. Tarn, F. Huang, J. Fan, *Particuology* **2015**, *19*, 1.

[28] R. Vyas, V. Lakafosis, H. Lee, G. Shaker, L. Yang, G. Orecchini, A. Traille, M. M. Tentzeris, L. Roselli, *IEEE Sens. J.* **2011**, *11*, 3139.

[29] M. Bissannagari, J. Kim, *Ceram. Int.* **2015**, *41*, 8023.

[30] D. Hrakova, P. Ripka, A. Laposa, D. Novotny, J. Kroutil, V. Povolný, O. Kaman, P. Veverka, *J. Magn. Magn. Mater.* **2022**, *563*, 170003.

[31] E. Enuka, M. A. Monne, X. Lan, V. Gambin, R. Koltun, M. Y. Chen, in *Quantum Sens. Nano Electron. Photonics XVII* (Eds: M. Razeghi, J.S. Lewis, G.A. Khodaparast, P. Khalili), SPIE, San Francisco, California **2020**, p. 58.

[32] L. Wu, J. Li, C. Liu, R. Zheng, J. Li, X. Wang, M. Li, J. Wei, *Phys. Lett. A* **2021**, *404*, 127406.

[33] D. S. Kolchanov, V. Slabov, K. Keller, E. Sergeeva, M. V. Zhukov, A. S. Drozdov, A. V. Vinogradov, *J. Mater. Chem. C* **2019**, *7*, 6426.

[34] H. Song, J. Spencer, A. Jander, J. Nielsen, I. Stasiak, V. Kasperchik, P. Dhagat, *J. Appl. Phys.* **2014**, *115*, 17E308.

[35] G. D. Han, K. C. Neoh, K. Bae, H. J. Choi, S. W. Park, J.-W. Son, J. H. Shim, *J. Power Sources* **2016**, *306*, 503.

[36] J. Ghogomu, E. Nforna, J. Lambi, *Am. Chem. Sci. J.* **2016**, *15*, 1.

[37] K. N. Al-Milaji, R. L. Hadimani, S. Gupta, V. K. Pecharsky, H. Zhao, *Sci. Rep.* **2019**, *9*, 16261.

[38] P. Tiberto, G. Barrera, F. Celegato, M. Coïsson, A. Chiolerio, P. Martino, P. Pandolfi, P. Allia, *Eur. Phys. J. B* **2013**, *86*, 173.

[39] P. Galizia, C. Baldisserri, C. Capiani, C. Galassi, *Mater. Des.* **2016**, *109*, 19.

[40] S. S. Shinde, K. M. Jadhav, *Mater. Lett.* **1998**, *37*, 63.

[41] M. Basak, M. L. Rahman, M. F. Ahmed, B. Biswas, N. Sharmin, *J. Alloys Compd.* **2022**, *895*, 162694.

[42] B. G. Toksha, S. E. Shirsath, S. M. Patange, K. M. Jadhav, *Solid State Commun.* **2008**, *147*, 479.

[43] A. Virden, S. Wells, K. O'Grady, *J. Magn. Magn. Mater.* **2007**, *316*, e768.

[44] S. Guchhait, H. Aireddy, A. K. Das, *Sci. Rep.* **2021**, *11*, 22890.

[45] K. Khaja Mohaideen, P. A. Joy, *J. Magn. Magn. Mater.* **2014**, *371*, 121.

[46] K. Maaz, A. Mumtaz, S. K. Hasanain, A. Ceylan, *J. Magn. Magn. Mater.* **2007**, *308*, 289.

[47] Y. C. Wang, J. Ding, J. H. Yin, B. H. Liu, J. B. Yi, S. Yu, *J. Appl. Phys.* **2005**, *98*, 124306.

[48] P. Galizia, M. Cernea, V. Mihalache, L. Diamandescu, G. Maizza, C. Galassi, *Mater. Des.* **2017**, *130*, 327.

[49] Z.-X. Tao, L.-Z. Li, X.-H. Wu, X.-X. Zhong, Z.-C. Zhong, *Phys. B Condens. Matter* **2021**, *604*, 412655.

[50] M. Dondi, F. Matteucci, D. Gardini, M. Blosi, A. L. Costa, C. Galassi, G. Baldi, A. Barzanti, E. Cinotti, *Adv. Sci. Technol.* **2006**, *51* 174.

[51] D. Gardini, M. Dondi, A. L. Costa, F. Matteucci, M. Blosi, C. Galassi, G. Baldi, E. Cinotti, *J. Nanosci. Nanotechnol.* **2008**, *8*, 1979.

[52] D. Gardini, M. Blosi, C. Zanelli, M. Dondi, *J. Nanosci. Nanotechnol.* **2015**, *15*, 3552.

[53] G. L. Güngör, A. Kara, D. Gardini, M. Blosi, M. Dondi, C. Zanelli, *Dye. Pigment.* **2016**, *127*, 148.

[54] G. Baldi, M. Bitossi, A. Barzanti, Ceramic Colorants in the Form of Nanometric Suspensions, **2008**, US7316741B2.

[55] P. Zaumseil, *J. Appl. Crystallogr.* **2015**, *48*, 528.